Fourth International Symposium on Marine Propulsors
smp'15, Austin, Texas, USA, June 2015

Large Eddy Simulation of a Cavitating Propeller Operating in Behind Conditions with and without Pre-Swirl Stators

Rickard E Bensow

Department of Shipping and Marine Technology Chalmers University of Technology, Gothenburg, Sweden

ABSTRACT

The hull-propeller interaction of a single-screw transport ship is investigated in model scale using large-eddy simulation in both a baseline configuration and one with a pre-swirl-stator installation. Simulations are performed for both non-cavitating and cavitating conditions. The analysis is focused on the unsteady effective wake, its impact on the propeller, and how this is affected by the installation of the stator blades upstream the propeller.

A complete geometrical model of the propeller is included in the simulations using sliding interfaces. Computed quantities include the time-resolved thrust, torque and side forces on the propeller, as well as the load on individual blades. The simulated unsteady flow field in the stern region and around the propeller blades is studied in detail for the wetted conditions. Results are also provided for the cavity extent in both configurations. Limited comparison with experimental measurements is carried out both for the flow field and forces on the propeller. A discussion is included concerning some differences noted between the baseline and the stator configuration and how that potentially impacts propeller design considerations and system performance.

Keywords

Cavitation, Energy Saving Devices, self-propulsion, LES

1 INTRODUCTION

Increasing requirements on ship propulsion performance puts increasing requirements on detailed knowledge on the propulsor hydrodynamics, and more and more interest is turned towards issues related to cavitation induced erosion, vibration, and noise. Thus, a detailed understanding of the hydrodynamics of hull-propeller-rudder interaction is of primary importance for a successful propulsion system design. The two most important objectives in the design of marine propulsors are most often high propulsive efficiency and low levels of vibrations and noise. Depending on vessel type, the related requirement on cavitation-free speed may also have a high priority. For cargo vessels, which is the focus for this paper, propulsive efficiency is typically most important, but induced vibrations and noise cannot be ignored during the design procedure. To improve system performance, there is currently a large interest in what is called ESDs, Energy Saving Devices, that should be designed to reduce hydrodynamic losses in the propulsion system and utilise the interaction effects between the hull, propeller, rudder, and the ESD itself. This forms a special challenge, both regarding the understanding of the interaction between components, as well as on the simulations tools that are necessary to use in the design process.

Traditionally, propulsion system performance is assessed through model tests or, to an increasing degree, RANS computations. With the continually increasing computational capacity, RANS computations for design purposes are today more and more becoming feasible to perform in full scale, making significant improvements possible in vessel design and power prediction. For the design of ESDs, the actual flow in full scale is crucial for its function and simulations are necessary in the design process. However, the assessment regarding induced vibrations and noise using RANS is limited, since it is based on the average flow field. As was elucidated in detail in Liefvendahl and Bensow (2014), the operating environment for the propeller is instantaneously very different from the average conditions. To reliably assess these issues, the full transient flow needs to be considered, which is becoming possible today with large-eddy simulation (LES) techniques, at least in model scale. Although such simulations generally are too costly for an iterative design procedure, we find that performing this type of analysis greatly improves the understanding of the flow and will contribute in the design of a well performing vessel.

This paper extends the scope of Liefvendahl and Bensow (2014) in two areas: First, we assess the impact of an ESD in the form of a pre-swirl stator installation, a PSS, upstream of the propeller that significantly changes the propeller inflow. Secondly, we look at the cavitation behaviour in both the baseline configuration and with the PSS.

In the present study, we provide an analysis of the hydrodynamic hull-propeller-rudder interaction for a 7000 DWT (Dead-weight tonnage) chemical tanker, which has been investigated within the framework of an EU-project (see below). The tanker is fitted with one four-bladed propeller and a standard spade rudder. The analysis presented in this paper is mainly based on implicit large-eddy simulations of the ship in self-propulsion, including the rudder and a complete geometrical model for the rotating propeller, with and without the PSS, and in both wetted and cavitating conditions. The water surface is approximated with a symmetry plane at the nominal water line. Cavitation simulations have been performed using the Kunz mass transfer model. The hull-propeller simulations are complemented by simulations of the towed hull condition and the propeller in open water. The simulations have been carried out in model scale and in slightly different conditions compared with model tests due to different objectives within the research project, limiting the possibilities to do detailed validation of the computations, but a general discussion on the reliability of the simulations and how the results compare to model test are included in Liefvendahl and Bensow (2014).

Using LES, we can study the time-resolved quantities related to this flow,their origin and their implications on operation of the propulsor system. The individual blade loads are analysed and we find a significant variation around an average due to the unsteady wake behaviour. Although an unsteady RANS simulation would include the basic varying blade loading, the representation of the flow over the hull would be steady and the wake inflow to the propeller smooth, with the transient behaviour induced only by the propeller. The LES thus provides far better possibilities to correctly assess propeller induced vibration and noise, as well as the hydrodynamic properties of the aft ship design and the propeller operating conditions in order to achieve best performance.

The paper is organised as follows. We begin by introducing the hull-propeller configuration and the operating conditions used for this study. We then present the computational methodologies used for the simulations. In the result sections that follow, we first briefly present results for the flow around the towed hull and a simulation of the propeller in open water conditions for the same operating point as in the self-propelled simulations. Then follows the focus of the paper, the detailed analysis of the fluid dynamics of the hull-propeller interaction, the resulting propeller forces and individual blade loading, comparing the baseline and the PSS configurations but also relate to the results of the open-water condition. Finally, we present the results from cavitating conditions for the two self-propelled configurations.

Table 1: Main model scale dimensions (scale factor $\lambda = 16.5$).

Quantity	Notation	Value
Length	L_{PP}	5.697 m
Beam overall	B	0.935 m
Draft	T	0.364 m
Wetted surface	S_0	8.335 m^2
Propeller diameter	D_p	0.233 m
Rudder span	R_s	0.247 m
Rudder chord	R_c	0.145 m

2 THE STREAMLINE TANKER

The configuration investigated here is a 7000 DWT chemical tanker of a standard design, similar to modern vessels but this particular hull has not been built in full scale. It is a single screw vessel, driven by a fixed pitch four-bladed propeller, which has been investigated within the framework of the EU-project STREAMLINE[1]. All results in the present paper have been obtained in model scale. The main hull particulars are given in Table 1, and the hull and propeller are visualised in Figure 1.

In project STREAMLINE, the flow around the tanker was investigated both for a baseline and the pre-swirl stator configurations, as is the case in this work, but an extensive campaign was also performed where hull and propeller were optimised and several different energy saving devices were designed for the vessel, including both pre- and post-swirl devices. Experiments have been performed both at CNR-INSEAN[2] and at CTO[3]. For this experimental campaign, the model was tested in the towing tank for resistance prediction and in the large circulating water channel for measuring the wake field by LDV in self propulsion conditions, as well as making cavitation observations and hull pressure measurements. The open water characteristics of the propeller was also measured in the towing tank. Published work from these studies are primarily the experimental study on propulsor-hull interaction by Pecoraro et al. (2013) for the baseline configuration and (primarily numerical) studies on the extended configurations, e.g. Deng et al. (2013); Queutey et al. (2013); Van der Ploeg and Foeth (2013); Calcagni et al. (2014); Bugalski and Szantyr (2014). The pre-swirl stators used were design within the project as a test configuration, and is composed of three stator blades on the port-side only. For simplicity, the profile of the blade sections was considered symmetric, made up of a NACA65 profile. The span of the stator blades is $0.55\ D_p$, measured

[1]Grant agreement 233896, European Union 7th Framework Programme.
[2]Istituto nazionale per studi ed esperienze di architettura navale, Italy.
[3]Centrum Techniki Okretowej S.A., Poland.

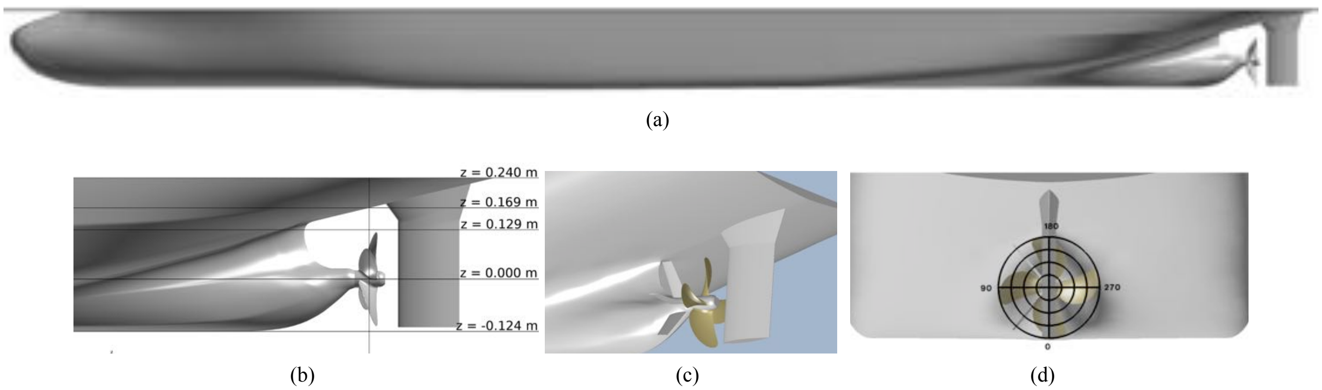

Figure 1: The STREAMLINE tanker and propeller. (a) Side view. (b) Zoom in the stern regions, with coordinates of the propeller plane and a number of vertical planes indicated. (c) Perspective view of the stern. (d) Rear view, which also illustrates the definition of the angle, φ, used to indicate the position of the propeller blades and stator blades.

Table 2: Operating conditions for the self-propulsion simulations.

Quantity	Notation	Value
Ship speed	V_m	1.773 m/s
Froude number	Fn	0.24
Propeller revolution	n	8.92 rps
Cavitation number	$\sigma_{N,m}$	1.18

from the shaft centre line, and the axial distance between the propeller and the stator is $0.3\,D_p$. The blades are positioned at 40°, 90°, and 140°, following the definition in Figure 1d; the angle of attack it set to 5° with respect to zero trim condition.

We will henceforth use the denotation BL for the baseline configuration and PSS for the pre-swirl stator configuration when presenting results in this paper. By Froude scaling, the full-scale speed is given by, $V_0^{(f)} = \sqrt{\lambda} V_0$. This corresponds to a speed of the full-scale vessel of 14.0 knots (at Fn $= 0.24$), which is the design speed. The propeller rotational speed, as well as environmental conditions, corresponds to measured values at self-propulsion in the circulating water channel at CNR-INSEAN. For this study, the rotational speed was kept the same in both BL and PSS simulations, but in reality this would have been adjusted for the PSS. The implications of this will be further discussed in relation to the results.

A cartesian coordinate system is used which has the origin at the stern of the hull. The x-axis is directed along the hull in the ship-forward direction with, $x = 0$, at the rudder stock. The y-axis is directed to the port side with, $y = 0$, on the symmetry plane of the hull. The z-axis is directed vertically upwards with, $z = 0$, at the propeller axis. In Figure 1b, the coordinate system is shown relative to the hull for the zero trim and sinkage condition. For the presentation of propeller results, we also use a polar coordinate system, (r, φ). The radius, $r = 0$, corresponds to the propeller axis and, $\varphi = 0$, corresponds to the vertically downwards direction. The angle increases in the direction of rotation of the propeller. The polar coordinate system is illustrated in Figure 1d.

3 SIMULATION METHODOLOGY

In this section, we briefly describe the main components of the complete algorithm used in this paper to compute the flow around the hull-propeller configuration under study. We also provide references to more complete presentations of the computational methods involved. Furthermore, the section includes information concerning mesh generation and other pre-processing of the simulations.

3.1 Large-eddy simulation

The conventional way of deriving the LES equations is to apply a low-pass filtering operation to the incompressible Navier-Stokes equations. Neglecting the terms stemming from the fact that, generally, differentiation and filtering do not commute, we obtain,

$$\begin{aligned} \frac{\partial \overline{\mathbf{v}}}{\partial t} + \nabla \cdot (\overline{\mathbf{v}} \otimes \overline{\mathbf{v}}) &= -\frac{1}{\rho}\nabla \overline{p} + \nabla \cdot (\overline{\mathbf{S}} - \mathbf{B}), \\ \nabla \cdot \mathbf{v} &= 0. \end{aligned} \tag{1}$$

where $\overline{\mathbf{v}}$ is the (filtered) velocity field, ρ the density, $\overline{p}$ the pressure, $\overline{\mathbf{S}} = 2\nu\overline{\mathbf{D}}$ the viscous strain tensor, $\overline{\mathbf{D}} = \frac{1}{2}(\nabla\overline{\mathbf{v}} + \nabla\overline{\mathbf{v}}^T)$ the rate of strain tensor, and ν the kinematic viscosity. The term in equation (1), arising from the filtering, is the subgrid stress tensor $\mathbf{B} = \overline{\mathbf{v} \otimes \mathbf{v}} - \overline{\mathbf{v}} \otimes \overline{\mathbf{v}}$. Here, variables with overbar denote filtered quantities. We refer to Sagaut (2002) as a general reference for LES and Fureby (2008), and the references therein, for LES applied to problems in naval hydrodynamics.

The LES modelling consists of deriving a computable expression for **B**. In these simulations we have used a mixed formulation of the subgrid stress term following Bensow and Fureby (2007), retaining the scale similarity term of the subgrid stress in the momentum equations. Further, for the remaining dissipative term, we have used implicit LES, which relies on the numerical diffusion to mimick the this action of the turbulence, see e.g. Grinstein et al. (2007). Several validation examples of these modelling techniques can be found in Fureby (2008) and for its application in cavitating flows, Bensow and Bark (2010) is one of many examples. In the remaining sections of the paper, we drop the overline notation for filtered quantities.

In LES for ship hydrodynamics, even at model scale, it is necessary to apply near-wall modelling (NWM) instead of resolving the largest turbulent structures in the turbulent boundary layer, as these become gradually smaller as the hull is approached. A wall-resolved LES-approach would lead to grid resolution requirements which increase faster with increasing Re-number for the boundary layer than for the turbulent regions away from the walls (Chapman, 1979). Such NWM is typically based on statistical arguments together with the mean velocity profiles of the viscous sub-layer and the logarithmic region of the turbulent boundary layer (Piomelli and Balares, 2002). The majority of these methods require the mean wall shear stress to be specified and used to adjust the velocity boundary condition.

We, however, use a method which modifies the subgrid viscosity close to the wall, as described in Fureby et al. (2004). The basis is the filtered boundary layer equations, which through the simplification of assuming zero streamwise pressure gradient and convective transport, integrate analytically to the logarithmic law-of-the-wall. This relation is the used to modify the subgrid model by adding a subgrid wall viscosity, ν_{NW}, to the kinematic viscosity so that the effective viscosity becomes,

$$\nu + \nu_{NW} = \tau_w / (\partial v / \partial y)_P = u_\tau y_P / v_P, \tag{2}$$

where the subscript P denotes evaluation in the first cell center next to the wall, y is a local wall-normal coordinate and v is the tangential velocity component. In Equation (2), the friction velocity, u_τ, is obtained either from the log-law or, preferably, from Spaldings law of the wall which incorporates also the buffer layer; this latter approach was used in this work. Since the model's only direct influence is on the subgrid viscosity, it can be combined with any other subgrid model.

3.2 Multiphase modelling

To simulate cavitating flows, the two phases, liquid and vapour, need to be represented in the problem, as well as the phase transition mechanism between the two. Here, we consider a one fluid, two-phase mixture approach, introduced through the local vapour volume fraction and having the spatial and temporal variation of the vapour fraction described by a transport equation including source terms for the mass transfer rate between the phases. Adding this transport equation to the filtered equations of continuity and momentum, Equation 1, we get (with over line filtering notation removed),

$$\begin{aligned} \frac{\partial(\rho \mathbf{v})}{\partial t} + \nabla \cdot (\rho \mathbf{v} \otimes \mathbf{v}) &= -\nabla p + \nabla \cdot [\rho\, (\mathbf{S} - \mathbf{B})], \\ \frac{\partial \rho}{\partial t} + \nabla \cdot (\rho \mathbf{v}) &= 0, \\ \frac{\partial \alpha}{\partial t} + \nabla \cdot (\alpha \mathbf{v}) &= {}^{\dot{m}}/_{\rho_v}. \end{aligned} \tag{3}$$

The density ρ and dynamic viscosity μ in Equation 3 are assumed to vary linearly with the vapour fraction,

$$\begin{aligned} \rho &= \alpha \rho_v + (1-\alpha)\rho_l, \\ \mu &= \alpha \mu_v + (1-\alpha)\mu_l, \end{aligned} \tag{4}$$

with the bulk values, ρ_v, ρ_l, μ_v, and μ_l, kept constant. Using this expression for the density in the continuity equation it's straight forward to derive the non-homogeneous velocity divergence due to the mass transfer between the phases,

$$\nabla \cdot \mathbf{v} = \left(\tfrac{1}{\rho_v} - \tfrac{1}{\rho_l}\right) \dot{m}, \tag{5}$$

that implies that the pressure equation in the PISO algorithm needs to be modified as well.

The mass transfer model used in this study is the one of Kunz et al. (2000). It uses different strategies for vaporisation and condensation, compared with most similar models that only rely on a single expression for both creation and destruction of vapour. The vaporisation, $\dot{m}^+$, is modelled to be proportional to the amount by which the pressure is below the vapour pressure and the amount of liquid present, while the condensation, $\dot{m}^-$, is based on a third order polynomial function of the vapour volume fraction,

$$\begin{aligned} \dot{m}^+ &= A^+ \rho_v (1-\alpha) \frac{\min[0, p - p_v]}{1/2 \rho_l U_\infty}, \\ \dot{m}^- &= A^- \rho_v (1-\alpha) \alpha^2, \end{aligned} \tag{6}$$

and the specific mass transfer rate is computed as $\dot{m} = \dot{m}^+ - \dot{m}^+$. Here, p_v is the vaporisation pressure and A^+ and A^- are empirical constants (of dimension $[s^{-1}]$). In these simulations, these parameters were set to $A^+ = 10^4$ and $A^- = 10^3$; no effort has been put into tuning them.. Thus, vaporisation occurs when the pressure is below the vapour pressure and there exist some liquid to vaporise, while condensation is restricted to the interface region of the cavity, independent of the pressure, with a maximum at $\alpha = 1/3$ and going to zero in the pure vapour region and the pure liquid region. The properties of $\dot{m}$ are thus such that the vapour fraction should stay in the interval $\alpha \in [0,1]$, but in the numerical solution procedure this is however not guaranteed. In our simulations, this has not been a problem and no limiting procedure on α has been applied.

3.3 The finite-volume method and the pressure-velocity coupling

The governing equations are discretised using the finite volume method and the unknown flow variables are stored in the cell-center positions in the computational grid. The algorithm supports arbitrary polyhedral cells and the grid is treated as unstructured. The approximations involved are of second-order accuracy, except for flux limiting for the convective term, which reduces locally the formal order of accuracy near sharp gradients. The momentum equation is treated in a segregated manner, solving sequentially the three components of the momentum equations in a loop within each time step. As the blade tip velocity imposes a Courant number (Co) restriction that is not directly related to the turbulent flow time scales, the simulations have been run with the so called PIMPLE algorithm in OpenFOAM for the coupling between the velocity and the pressure fields, allowing for stable transient simulations with $Co \geq 1$ (in this case the maximum $Co \approx 2.5$). The PIMPLE algorithm is a merge of the SIMPLE (Patankar and Spalding, 1972) and PISO algorithms, where the PISO loop is complemented by an outer iteration loop and possible under-relaxation of the variables, see e.g. Barton (1998) for different ways to merge PISO and SIMPLE procedures. For the cavitating flow simulations, the mass transfer sources are computed first in the PISO loop, then the vapour fraction transport is progressed, and finally the standard PISO procedure is entered.

The simulations are time resolved and a second order backward differencing scheme is used for the time advancement of the components of the momentum equation, as well as for the time advancement of possible additional transport equations associated with the sub-grid modelling described below. A domain decomposition technique, applied to the grid, in combination with an efficient MPI-implementation is used for running on parallel computers. The solvers which are used are implemented using the open source software package OpenFOAM, which provides an object-oriented library, based on the finite-volume method, specifically designed for CFD. See Weller et al. (1997), for a description of the structure of this software design.

3.4 Dynamic grid methods and mesh generation

The inclusion of a moving component (in this case the propeller) is significantly more complex from an algorithmic point of view as compared to fixed grid simulations. Here, the sliding-interface implementation recently introduced in OpenFOAM has been used, where in this case a cylindrical region enclosing the propeller is introduced, which rotates rigidly with the propeller, and interpolation is performed between the non-conforming sliding interfaces between the two regions. The implementation is based on the interpolation algorithm by Farrell and Maddison (2011), denoted as AMI (Arbitrary Mesh Interface). This constitutes an efficient and conservative interpolation between non-conforming mesh interfaces based on Galerkin projection. The AMI has been shown to show good performance regarding both scalability and conservation of the flow quantities (Bensow, 2013; Turunen, 2014).

A primarily unstructured mesh approach was adopted, except around the propeller. Two subregions are used, one fixed for the hull and one rotating cylinder around the propeller; the latter indicated by the red box in Figure 2. To achieve a well controlled resolution around the propeller, a structered hex mesh was first created around the blades, then the rest of the rotating cylinder domain was filled with unstructed tet elements, interfaced by pyramid elements (listed as polyhedral in Table 3). For the hull, a triangular surface mesh was created from which a prismatic boundary layer mesh was extruded before the rest of the domain was filled with tet elements. The number of cells of different types is given in Table 3. The mesh resolution is decent for a model scale LES, with typical cell sizes in the aft body boundary layer and on the propeller of $(\Delta x^+, \Delta y^+) = (100, 5)$, where Δx^+ represents the longest surface cell edge and Δy^+ the wall normal cell size.

3.5 Other simulation parameters and pre-processing

The time advancement parameters and pre-processing associated with force computation are described in this section. Table 4 summarises the time step and the important time in-

Table 3: Number of cells in the computational grids for the BL configuration, according to cell-type.

#cells/10^6	Hull	Propeller	Total
Hex	-	1.25	1.25
Tet	6.34	6.07	12.41
Prism	5.78	0.04	5.82
Poly	0.08	0.06	0.14
Total	12.2	7.42	19.63

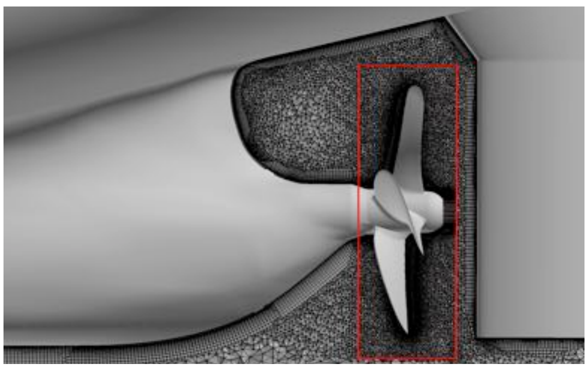

Figure 2: Illustration of the aft ship mesh, where the red box indicates the boundary of the rotating cylinder mesh where the sliding mesh interface is applied.

stants for simulations. Simulations were first performed for the towed BL configuration without the propeller. The propeller was then added to the fully developed flow and the simulation was further run to remove initial transients in the flow field before sampling was started. At the end, the simulation was further run in cavitating conditions. The simulations of PSS configuration was started from the BL simulations. The number of samples for collecting average data is clearly limited, and expected to only give some indicative impression of the average flow field.

At each time step of the simulations, the fluid force and moment are integrated over certain areas (patches) of the hull, propeller and rudder surfaces. Each propeller blade corresponds to one patch, the propeller hub, the hull and the rudder constitute the remaining patches. The simulations thus provides the complete time history of these forces. The moments are computed with respect to a point on the propeller axis.

Let $\mathbf{T}(S,t)$ denote the force on patch S at time t, and $\mathbf{Q}(S,t)$ the moment. For the propeller we include the blades, but not the hub, in the computation of propeller thrust and

Table 4: Time advancement parameters. The time step, Δt, is given both in mikroseconds and degrees of propeller rotation. The start time of the simulation is denoted T_0, T_1 is the time instant when the start-up transients in the propeller forces have passed, T_2 the end time of the simulation in wetted conditions and cavitating conditions initialised, and finally T_3 the end time of the simulations..

Quantity	BL	PSS
$\Delta t(\mu s)$	15.6	15.6
$\Delta t(^o)$	0.05	0.05
T_0(s)	0.00	0.00
T_1(s)	0.48	0.11
T_2(s)	1.24	0.43
T_3(s)	1.43	0.53
$(T_2-T_1)/T_{rot}$	6.78	2.85
$(T_3-T_2)/T_{rot}$	1.71	0.89

torque. If S_p denotes the propeller, then the conventional non-dimensional coefficients for thrust and torque are given by,

$$K_T(t) = -\frac{\mathbf{T}(S_p,t)\cdot\mathbf{e}_x}{\rho n^2 D_p^4}, \qquad K_Q(t) = \frac{\mathbf{Q}(S_p,t)\cdot\mathbf{e}_x}{\rho n^2 D_p^5}.$$

The unit vectors in the three coordinate directions are denoted by, $\mathbf{e}_x$, $\mathbf{e}_y$ and $\mathbf{e}_z$ respectively. Results will also be presented for the transversal and vertical forces on the propeller, for which we use the non-dimensional coefficients,

$$K_{Ty}(t) = \frac{\mathbf{T}(S_p,t)\cdot\mathbf{e}_y}{\rho n^2 D_p^4}, \qquad K_{Tz}(t) = \frac{\mathbf{T}(S_p,t)\cdot\mathbf{e}_z}{\rho n^2 D_p^4}.$$

For the axial load on an individual blade, we employ the corresponding coefficient,

$$K_{Tb}(t) = -\frac{\mathbf{T}(S_b,t)\cdot\mathbf{e}_x}{\rho n^2 D_p^4},$$

where S_b is the patch of the propeller blade.

4 BARE HULL FLOW

Here, we present results on a the BL configuration in towed condition, i.e. without propeller operating. The operational conditions and simulation parameters are otherwise the same as for the self-propulsion simulation. Also the mesh is identical outside the propeller cylinder, which here was replaced by a mesh matching the rest of the stern region in size and type.

With a view to basic qualitative validation of the simulations with experimental data and further the flow conditions of importance for propeller operation, we now provide a brief

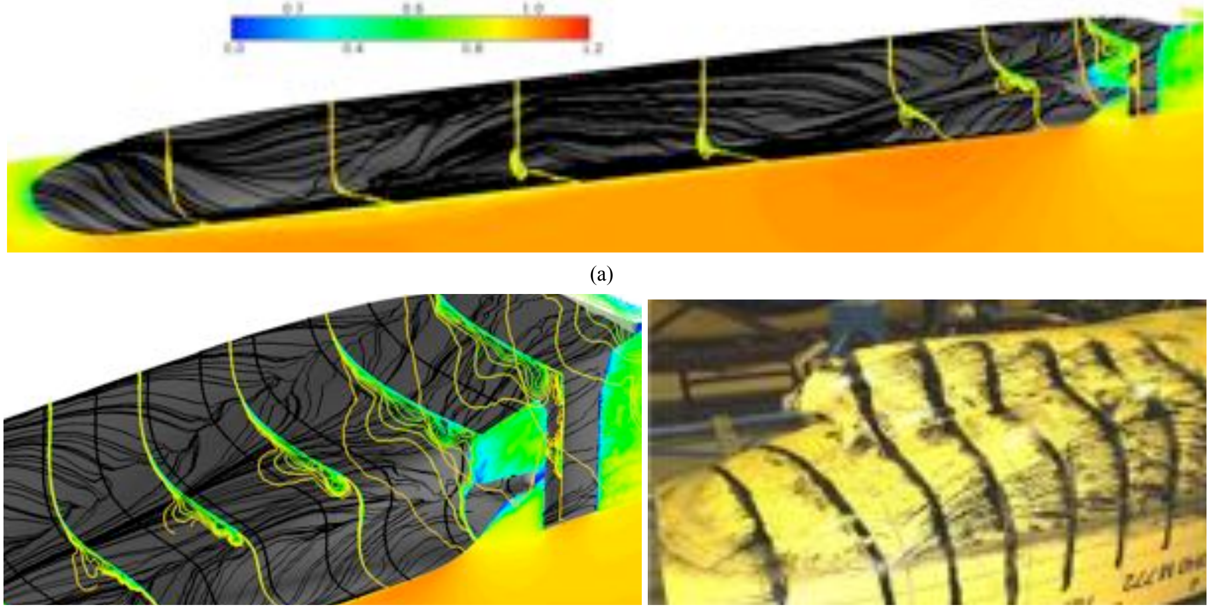

(a)

(b) (c)

Figure 3: Overview of the flow for the towed hull. In (a) and (b), the normalised instantaneous axial velocity is plotted on the center plane and in cross-planes. Furthermore, the surface streamlines, also based on instantaneous velocity, are shown in black. (c): Paint visualisation from towing tank experiments

overview of the flow around the towed hull. Further detailed discussion on the wake flow is however focused on the effective wake and thus postponed to the later section where the simulations of the full configurations are presented. In Figure 3, we show visualisations of the flow and paint flow from towing tank experiments reported in Pecoraro et al. (2013). Along the hull, the flow is dominated by the pair of bilge vortices which are formed at the bow, extend along the hull, and separate slightly at the stern, passing well on the sides of the propeller disc. At the stern the flow becomes more complex as the adverse pressure gradient, caused by the hull curvature, decelerates the flow and a region of low flow velocity is created. Embedded into this region is the bilge vortex pair, as well as additional vortices created in the stern region. These vortices are indicated by surface streamline convergence in Figure 3.

The simulations indicate a shallow but significant unsteady flow separation on the hull after-body, just upstream of the propeller. Overall, the occurrence, shape and size of this predicted flow separation is in accordance to the findings and analysis based on the towing tank experiments (Pecoraro et al., 2013). This holds also for the development and position of the bilge vortices and the flow over the gondola. Hence this provides a qualitative validation of the large-eddy simulations and the further studies on the propeller flow and loading is relevant.

For the discussion of hull-propeller interaction further on, we also note the vertical component of the propeller inflow, visible from the flow development over the gondola. There is a reasonable agreement between both simulations and the experiments regarding this flow component and it is the explanation to several features regarding the propeller behaviour discussed below. It is of particular interest in the design and functioning of the pre-swirl stators.

5 OPEN WATER PROPELLER SIMULATION

The exact experimental configuration of the open-water test has not been reported. Normally, such a propeller test in a towing tank would be expected to be run with the propeller mounted upstream the shaft. As the geometrical details for the test are not known to us, the corresponding open-water simulation was set-up based on the self-propulsion configuration by using the same hub and cap and extending the shaft upstream. The simulated propeller thus operates pushing. We remark that the primary objective of the simulation is for qualitative comparison with the propeller operating in behind condition, and not to validate the computational technique. For

Table 5: Propeller thrust and torque in open water condition. Results from experiments and simulation.

$J = 0.629$	Exp.	LES
K_T	0.246	0.247
K_Q	0.406	0.411

this purpose we refer to Bensow and Liefvendahl (2008).

In this work, the only open-water simulation presented is for advance coefficient $J = 0.629$, which is the experimentally determined (through thrust identity) operating condition corresponding to the self-propulsion case at $V_0 = 1.773$ m/s. The simulation was performed using a mesh that around the propeller is indentical to the one used in the self-propulsion simulations. The blade wake is somewhat refined in the open-water case which is not expected to significantly alter the behaviour compared with the grid used in the self-propulsion simulation. The thrust and torque for the simulation are reported in Table 5 and they are in good agreement with experimental data. The flow around the blade is discussed in connection with the behind condition below.

6 THE COMPLETE HULL-PROPELLER-PSS CONFIGURATION

After the brief introduction of the flow around the towed hull and the propeller in open-water condition, we now come to the main focus of the present paper: An analysis of the hull-propeller interaction, and primarily on the difference between the BL and the PSS configurations. We start by a discussion of the inflow to the propeller and a comparison between the two configurations. The resulting mean forces and level of fluctuations of the forces on the propeller for the two simulated cases are then given. After this follows a detailed investigation of the blade load time histories and how to correlate this with the hull-propeller flow. We also consider the unsteady propeller dynamics, by analysing the flow around the blades at different loading condition, including a comparison with the open-water condition. The section is concluded with an overview of the cavitating behaviour in the two configurations.

6.1 The flow in the vicinity of the propeller

We noted above that the structure of the inflow to the propeller is strongly affected by the flow separation upstream of the propeller. The inclusion of the propeller leads to an acceleration of the flow upstream of the propeller, and a contraction of the low velocity region. The effect is rather localised and significant only within approximately one propeller radius upstream of the propeller plane. Hence the flow separation upstream of the propeller is still present in simulations. Moreover, the flow from below the hull, over the gondola and into the propeller leads to a vertical velocity component in the propeller inflow, greatly affecting the blade load variation during one propeller revolution as the blade experience following flow on its way upwards on the port side and opposing flow on its way down. This is particularly true in the BL configuration, while the stators in the PSS aim to change direction of this vertical component on the port side.

The inflow to the propeller is illustrated in the cross-plane plots of Figure 4. Shown in the figure is, for both BL and PSS, the axial and vertical flow components upstream of the propeller. Also shown in the figure is the velocity distribution just downstream of the propeller. The comparison is carried out using instantaneous data since no phase-averaging was included in the hull-propeller simulations for three-dimensional flow data. Naturally, there is a significant variation between instantaneous velocity distributions, but Figure 4 still provides an adequate illustration of the qualitative flow features discussed next. An impression of the instantaneous variation in inflow is given in Figure 9.

First we compare the axial velocity shown in Figure 4a of BL with that in Figure 4b, of the PSS. The most apparent feature that differs is of course the wake of the three stator blades. More interesting is perhaps that the sharp velocity deficit on the BL, due to the separation on the hull, is not present for the PSS. It thus appears that the separation zone just ahead of the propeller is affected by the PSS installation. By looking at the surface flow (not included in the paper), it is not possible to observe this difference, and it's not completely clear why this effect should be present. Further studies are needed to correctly explain this behaviour.

The effect of the stator blades to create pre-swirl can be seen by studying the differences between Figures 4 (c) and (d). For the left figure, the BL, the vertical component is clearly visible from the yellow and orange coloured contours on both port and star bord sides, while in the right figure, the PSS, the green on the port side indicate a close to zero vertical flow component. The tip vortices from the stator blades are also apparent, right on the perimeter of the propeller disc. Further, several secondary vortices created on the upstream foils can be detected.

Downstream the propeller, Figure 4 (e) and (f), the blade

Table 6: Propeller forces and torque. The experimental data is taken from self propulsion towing tank measurements. The definitions of the force coefficients are given in the pre-processing section.

	Mean			Std.dev	
	Exp.	BL	PSS	BL	PSS
K_T	0.250	0.247	0.284	0.0064	0.0044
$10K_Q$	0.413	0.396	0.449	- - -	- - -
K_{Ty}	- - -	−0.004	−0.002	0.002	0.002
K_{Tz}	- - -	0.022	0.018	0.008	0.002
K_{Tb}	- - -	0.062	0.071	0.015	0.010

wakes are clearly visible as well as the accelerated flow in the propeller slip. Note the difference between the two configurations, where for the BL the axial velocity is higher on the starboard side compared with the port side, mainly associated with the fact that there is a mean vertical component of the inflow to the propeller, which leads to higher blade load (and more flow acceleration) on the starboard side where the blade meets the vertical flow component. This effect is considerably reduced for the PSS, as the stators have removed this vertical component, as noted above.

6.2 Propeller forces

Statistics for the propeller thrust, torque and transversal forces, as well as the blade loads, are summarised in Table 6. The mean and the standard deviations have been calculated based on force time series according to Table 4 . We use $\langle\cdot\rangle$ to denote the mean of a quantity, and $\sigma(\cdot)$ for the standard deviation.

The computed mean thrust and torque show good agreement and are within 5% of the measured values for the BL simulation. The thrust delivered for the PSS is considerably higher, 13.3%, than the BL which is certainly higher than the additional resistance caused by the stator blades. It is thus clear that the rate of revolution should be reduced for this configuration or the propeller redesigned. The predicted thrust fluctuations, $\sigma(K_T)/\langle K_T\rangle$, are at 2.6% for BL and only 1.6% for PSS. Admittedly, the sampling time is short, in particular for the PSS, but the behaviour is very consistent giving belief that the results are indicative of the real situation. This indicates that although the stator blades introduces additional inhomogeneity in the propeller inflow, the global flow features in this configuration gives a considerably overall smoother thrust curve. The blade load fluctuations, $\sigma(K_{Tb})/\langle K_{Tb}\rangle$, naturally are significantly higher than the thrust fluctuations,

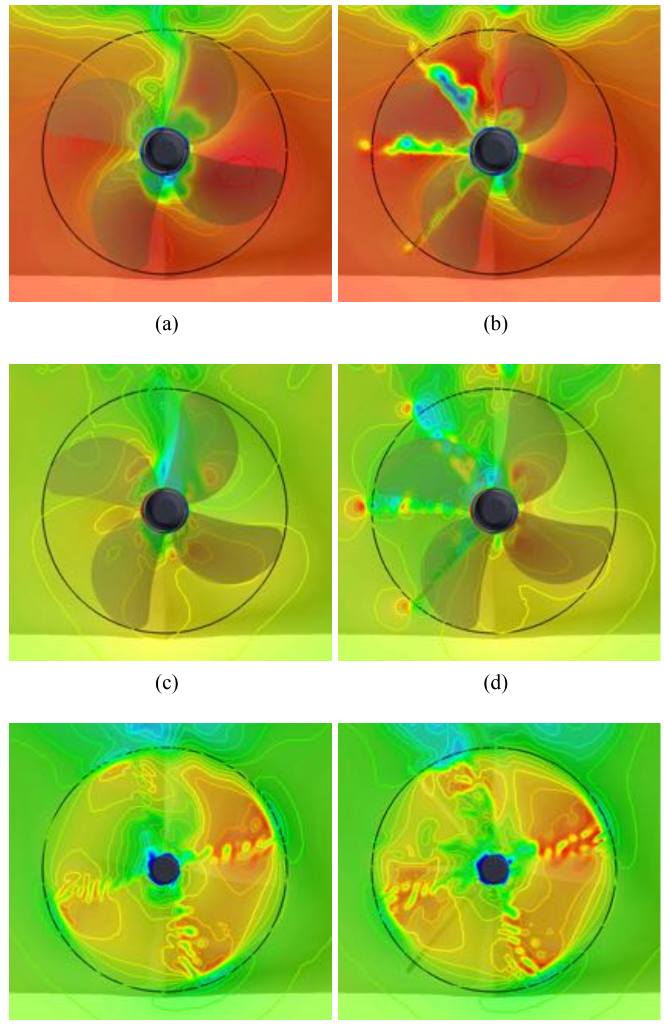

(a) (b) (c) (d) (e) (f)

Figure 4: Instantaneous normalized velocity. In the left column (a,c,e), the flow in the BL configuration is plotted, and in the right column (b,d,f) the PSS. In the top row (a,b), the normalised axial velocity in a cross-plane just upstream of the propeller at $(x - x_p) = 0.309R_p$; for the PSS this is right in between the trailing edge of the stators and the leading edge of the propeller. In the middle row (c,d), the normalised vertical velocity is plotted at $(x-x_p) = 0.309R_p$. In the bottom row, the normalised axial veolcity is plotted in a cross-plane just downstream of the propeller at, $(x - x_p) = -0.309R_p$. The black circles illustrate the propeller radius. Note that the color scale range varies: in the top row $\hat{U}_x \in [0,1]$, in the middle $\hat{U}_z \in [-0.5,0.5]$, and in the bottom $\hat{U}_x \in [0,1.5]$.

and we have 25% for BL and 16% for PSS. Another important observation in Table 6 is the significant mean vertical force component K_{Tz} on the propeller for BL, and the corresponding lower value for PSS. This is caused by the sloping hull above the propeller and the resulting inclination of the propeller inflow and the correction of this by the stator blades. For BL the prediction is, $\langle K_{Tz}\rangle/\langle K_T\rangle \approx 9\%$, and for PSS it is 6%. As elucidated below, this vertical force component is directly connected to the blade load variation during the rotation.

The blade load, K_{Tb}, is plotted as a function of rotation angle in Figure 5, for both configurations. Both the phase average and the instantaneous blade load curves are included. The qualitative behaviour of the phase-averaged curve is explained by variation of the axial velocity of the inflow (see Figure 4) and the fact that there is a mean vertical component of the inflow to the propeller. The lowest blade load for BL occurs at $\varphi \approx 70^o$, where the blade rotates upwards and the axial flow velocity is relatively high. For BL, the highest blade load occurs in the vertical position, $\varphi = 180^o$, or just after this, where the axial inflow velocity is very low. During the rotation from, $\varphi = 180^o$, to, $\varphi = 360^o$, the blade load falls off. Due to the vertical component in the inflow, there is a plateau with relatively high load with the blade to the starboard side, approximately in the interval, $200^o < \varphi < 330^o$. For PSS, the situation is different as the flow deflection of the stator blades removes the apparent minimum and instead bumps the thrust curve locally at $\varphi \approx 65^o$. Moreover, the maximum peak in the vertical position, $\varphi \approx 180^o$, is not present, as the velocity deficit in this region has disapperad, as was noted above. These two features are responsible for the lower blade thrust variation noted in the previous section.

Connecting this behaviour to vibrational considerations in the ship design, we note for BL both pulsating component due to the large variation in blade thrust from the minimum position around $\varphi \approx 70^o$ to the maximum at $\varphi = 180^o$. Moreover, the propeller shaft will experience an average torque towards port due the plateau in the thrust generated as the blade moves downward. This is visually also clear from Figure 4. This potential issue is significantly reduced for the PSS as both peaks are removed and the overlap of the blade forces results in a much more even total thrust curve.

6.3 Unsteady propeller dynamics in wetted conditions

The above discussion concerned primarily the statistics of the propeller forces, while we will here describe the flow field around a single propeller blade during one revolution in behind condition, discuss the details of the blade-to-blade variation, and compare between the two simulated configurations and the open water characteristics. The main variation is, as described above, due to the characteristics of the wake field from the hull, with the high velocity deficit in the top position and a slight overall vertical component as the fluid rises along the aft hull lines. In addition to this, we see the variation due to the wake unsteadiness, both with respect to its width and vortex content, as well as a slow movement from side to side. The actual stator wakes adds some details to the variation but does not give a major contribution.

In Figure 7, we relate the loading in behind condition to the open water characteristics of the propeller. Starting with the BL, the circle symbols in the figure, we note that at $\varphi = 0^o$, the bottom blade position, the loading condition is closest to open water condition with the K_{Tb} approximately one fourth of the total thrust coefficient, corresponding to $J = 0.654$ (through thrust identity). The blade then proceeds towards a lighter loading as it experiences a vertical flow component in the wake flow. Minimum loading is experienced at around $\varphi \approx 70^o$, before a step increase towards the peak in the maximum velocity deficit of the wake. Following that, we have above noted the plateau as the blade has moved out of the wake peak but instead is rotating towards the vertical flow component on the starboard side of the hull.

Turning to the PSS simulations, the filled diamonds, there are two features that clearly separate the behaviour from the BL. First, the propeller is higher loaded, with the points lying to the left of the corresponding points for BL; this is due to the simulations conditions using the same rate of revolution. More interesting is to note that the points are also more clustered, with smaller variation in effective advance coefficient. This should be possible to utilise in the design of the propeller and thus increase the average efficiency of the propeller.

We continue this section by a detailed discussion of the flow around the blades. The pressure field and surface streamlines on the blades are shown in Figure 8 for the positions at 0°, 90°, 180°, and 270°. Considering the blade in the vertically downwards position, the blade flow is as expected fairly similar to the open water condition.We note though that the low pressure region on the suction side tip of the blade is much shorter in the behind condition as the blade is moving towards the lighter loaded position. This is however compensated by higher pressure levels on the pressure side of the blade, giving the slightly higher loading compared with the open water condition. The pressure distribution of the BL and the PSS are rather similar, with perhaps a slightly larger region of low pressure for the PSS.

Looking now at the pressure side in the first rows of the figure,

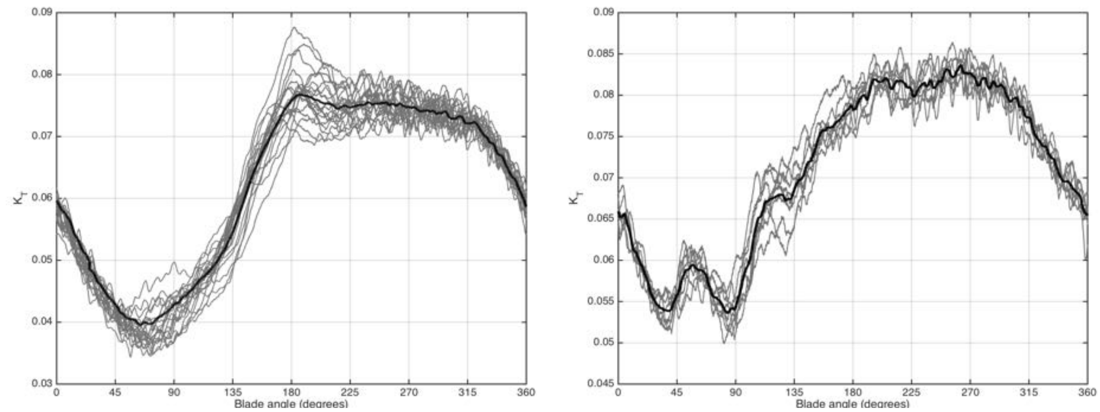

(a) (b)

Figure 5: Scatter plot of blade load, $K_{Tb}(\varphi)$, based on data for four blades and six propeller rotations for BL and two for PSS. The bold line represents the phase-averaged blade load; (a) Simulation BL; (b) Simulation PSS.

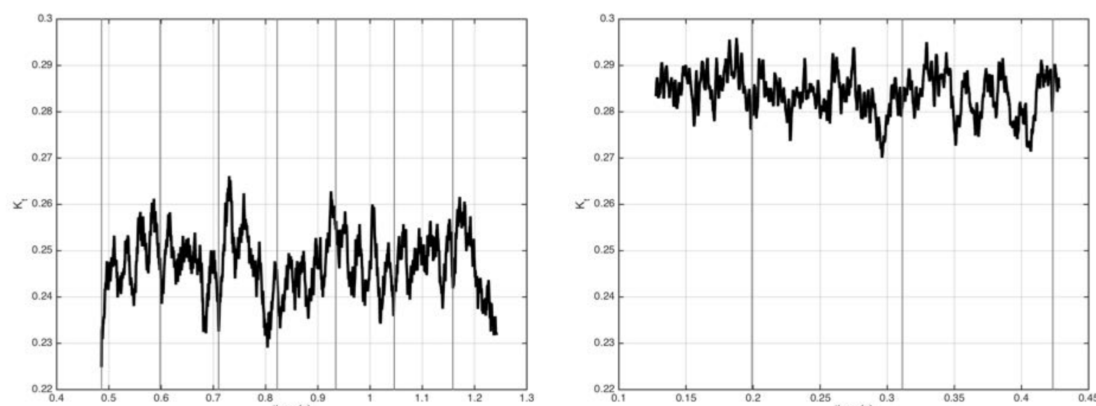

(a) (b)

Figure 6: Plot of the thrust, $K_T(t)$, for BL (above) and PSS (below). The vertical lines indicate time instants when the reference blade occupies the top position, $\varphi = 180$.

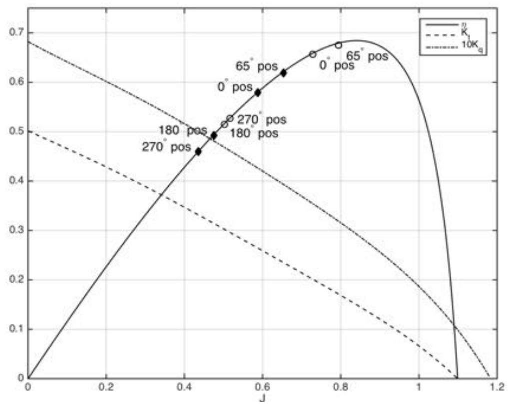

Figure 7: Phase average of blade load, at four selected angles, plotted in the open water diagram of the propeller for the two configurations. The points in the diagram represents the blade load multiplied by four, in order to correlate it with the thrust of the four-bladed propeller.

there are two notable features, both relating to the BL configuration. The first is what appears to be a pronounced pressure side vortex developing along the radii below, $r/R_P \approx 0.8$, as the blades moves from the bottom position to towards the top position, as is shown in Figure 8c. Relating this behaviour to Figure 7, we can indeed see that the blade is operating very close to the efficiency peak, and will certainly during some rotations pass over the peak. This is the effect of the following flow into the propeller causing a local unloading of the blade. The other feature is the large region of high pressure along the leading edge in the star bord position, shown in Figure 8e. We can also comment that there is a local small high pressure patch on the PSS in frame (g), due to the velocity deficit from one of the stator blades.

Turning to the suction side, Figure 8 bottom two rows, the main noticeable general features is the difference between the open water conditions and in behind regarding the region of flow separation towards the trailing edge. This flow separation is present to some degree already in the open water condition, but is much more pronounced at all instances when the propeller operates in behind condition. We clearly see the traces of smaller vortical structures in the pressure field, and this behaviour is believed to be responsible for the small high frequency oscillations in the individual blade loading seen in Figure 5. The reason for this discrepancy is not fully understood at the moment, but could be related to the disturbed inflow and the time history of the blade loading. Similar flow features as detected in the self propulsion conditions have been noted for laminar flow over propeller blades, and although in principle the LES could be able to capture this to some extent, it does not make sense that the propeller flow in behind conditions is more laminar than in open water. Another feature we can read from the surface streamlines is how they are deflected by the thickening tip vortex that develops during the previous quarter of a revolution.

Finally, we return to the cycle-to-cycle variation in thrust, this is related to the unsteady nature of the wake. Looking at Figure 5 again, we note some qualitatively different types of variations around the mean, apart from the small oscillations discussed above. The first, most prominent for the BL, is the variation in level in K_{Tb} primarily due to how large the velocity deficit in the wake is at that particular instant for the particular blade position. We here note a variation in the order of ±15%. This is most pronounced for the peak load at the top position and to a large extent also at the plateau, but to some extent, surprisingly enough, also in the bottom position. We note however that the flow analysis above indicate intermittent separation also towards to lower part of the gondola entering then the bottom blade position.

A second type of variation is the phase shift of the curves in Figure 5, clearly seen between blade positions of about, $\varphi \approx 60^o$, and, $\varphi \approx 200^o$ for the BL; in the case of PSS there is an indication of this behaviour as well but the statistics are too weak to say anything definitive. This is related to the wake velocity deficit moving laterally, with the blade then experiencing the maximum loading during the revolution not exactly at the top position, but with a variation for each blade passage. These kind of variations were discussed in some more detail in Liefvendahl and Bensow (2014).

For the PSS, we see a large variation in instantaneous axial velocity due to the flow structures developing on the stator blades. The most notable among the pictured instants in Figure 5 is in frame (g), where a large very low velocity structure is appearing on the middle stator blade. The time visualised in this figure and in Figure 8 are not correlated, but the effect of a similar structure is visible through the locally low pressure spot on the leading edge in Figure8p. Although this has not been detected in the cavitation simulation, it is expected that this behaviour very well could lead to cavitation of a problematic type.

Looking further to the difference between the BL and the PSS, also the flow close to the root of the blades show differences with the PSS case showing a less pronounced vortex system developing over the gondola and entering the propeller than the BL. This is an important difference, as the variation in this velocity deficit was noticed in Liefvendahl and Bensow

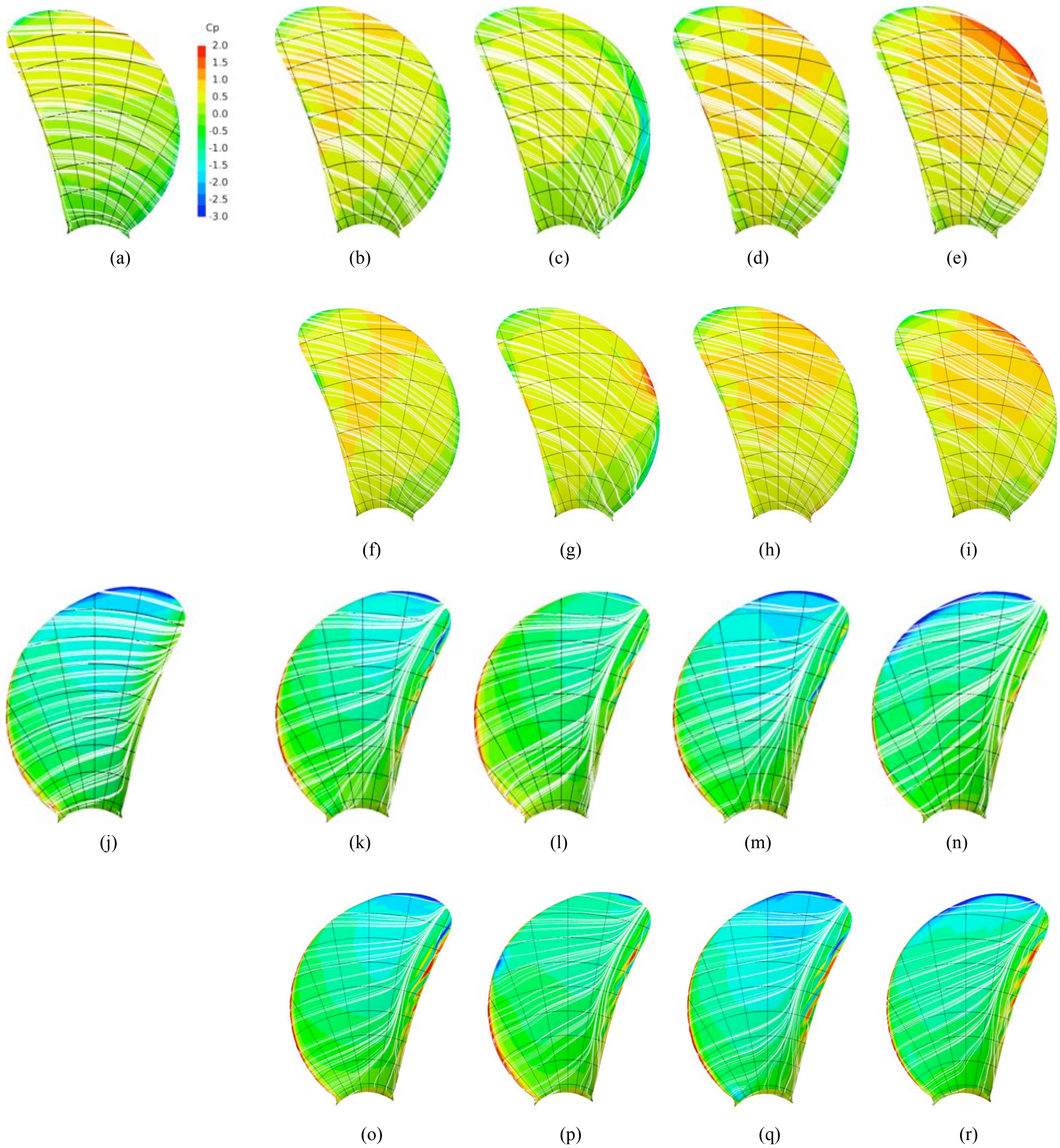

Figure 8: Contours of pressure coefficient, C_P, and surface streamlines on the pressure and suction side of the blade. The BL is shown in the first and third row and the PSS in the second and fourth, except for the first column where the open water propeller is shown. Panel (a): Open-water condition; figures (b), (f), (k), and (o) : blade vertically downwards, $\varphi = 0$; figures (c), (g), (l), and (p): blade to port side, $\varphi = 90^o$; figures (d), (h), (m), and (q): blade vertically upwards, $\varphi = 90$; figures (e), (i), (n), and (r): blade to star bord side, $\varphi = 270^o$. The scale used for C_P is shown in the panel (a) and is the same for all other images

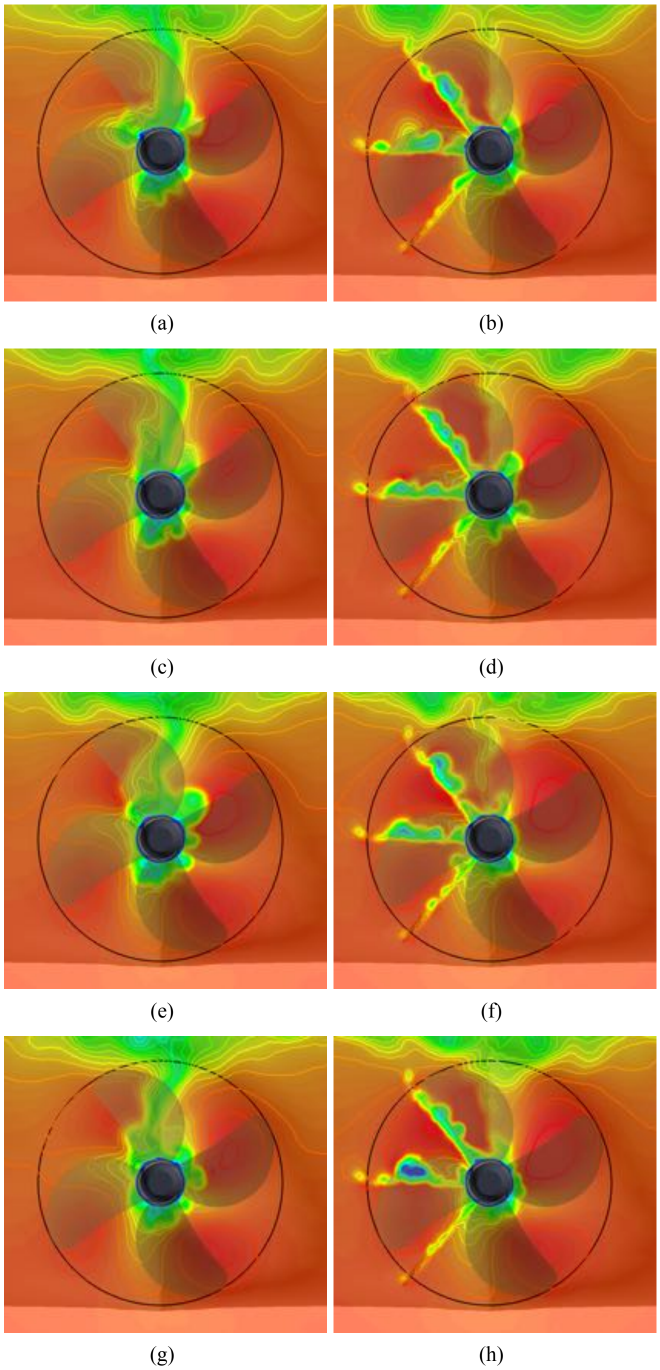

Figure 9: Wake inflow to the propeller during one revolution in BL (left column) and PSS (right column). The figure shows instantaneous normalised axial velocity in a cross-plane in between the propeller and the stator blades, at $(x - x_p) = 0.309R_p$, with the same colour scale as in Figure 4. Between the consecutive figures, the propeller rotates 90^o.

(2014) to be responsible for a significant part of the thrust variation we see in Figure 6. This is partly related to the apparently weaker separation on the hull over the gondola for the PSS, commented on above, but also the smaller separation zone below the gondola appears to be weaker for the PSS.

The description here has been made for only one realisation of rotation, but it is clear from Figure 5 that similar behaviour occurs for all rotations. For the BL, this variation has largest impact on the blade as it moves upwards to the top position, while the stator blades counteract this somewhat for the PSS. However, we remark that the the range of propeller positions spanning $\Delta\varphi \approx 25^o$ around the top position, there is a large variation in thrust for both configurations. The behaviour we see in these simulations, and illustrated in Figure 9, also indicates that the average wake width is considerably wider and smeared compared with the instantaneous, and that this is due to the constantly changing position of relatively thin flow structures in the instantaneous wake. This observation holds for both the BL and the PSS, although for the former it relates to the velocity deficit in the top positions and for the latter is concerns the stator blade wakes.

6.4 Cavitating Flow Behaviour

The original objective of this work in the STREAMLINE project was to study impact of the PSS on risk for cavitation erosion. Unfortunately, the geometries and conditions chosen in the project, as described above, resulted in a rather weak and intermittent cavitation on the propeller. The following section thus includes not a detailed assessment of the cavitation issues that can be expected on these kind of vessels, but rather a discussion on what kind of information that is possible to extract with modern simulation techniques.

The comparison with the experimentally observed cavitation is not straight-forward for several reasons, the two most prominent are that the tested conditions are different and that the cavitation is intermittent and depends on the instantaneous inflow from the hull; a detailed validation is thus out of the scope in this work. Due to technical problems, the cavitation test at the condition chosen (14 kns in full scale) for the simulation work in failed and data is only available at the neighboring thrust conditions of 13 kns and 15 kns. The simulations presented here were made for a cavitation number $\sigma_{N\_m} = 1.18$, where experimental images are available for the 13 kns condition; some snap-shots produced by CNR-INSEAN in the STREAMLINE project are replicated here in Figure 10 for comparison with the simulation results presented in Figures 11c and 11f. As a qualitative comparison, the agreement of on blade cavitation is reasonable while the simulation fails to predict the trailing tip vortex cavitation. This feature is not clear from the included experimental images and is weak in current conditions, but clearly visible at least for some time instances. The prediction of vortices is a well known difficulty due to numerical errors, and despite some mesh refinement in the tip vortex and blade wake regions this was apparently not sufficient.

From a potential erosion assessment of the flow, we observe a certain level of detail in the cavity formation and dynamics, indicating that the resolution probably is sufficient to have supported a certain level of visual assessment of erosion risk. We can identify that the tip vortex is lifted from the blade while exiting the wake peak, in some instances we note a break-up of the tip vortex, and we see a high degree of small scale structures along the trailing edge of the propeller blades; all phenomena perhaps best seen in Figure 14. Furthermore, we see vortex development over the suction side of the stator blades as the blade passage accelerates the flow, e.g. in Figure 13, also indicating that the resolution is fine enough to capture cavity dynamics and shed cavities if the loading had been higher. Overall, we also remark that we observe some differences in cavitation behaviour between different blade passages, indicative of the influence of the unsteady wake.

The differences between the BL and the PSS are minor. The stator blades counter act a vertical velocity component in the wake flow on the port side of the gondola, thus increasing the loading on the blades as they pass in the port position. This is not enough to trigger cavitation during the simulated revolution, but has an impact on the blade loading and the propeller thrust. Also, the low velocity burst from the stator blades, as noted above, does here not lead to any cavitation either. Furthermore, there are indications that the PSS reduce the flow separation visible on along the trailing edge of the propeller blades, but the simulation time is not long enough to confirm this.

Finally, we note the very large impact of the cavitation on the hull pressure. This has not been the focus of this investigation but we here comment on the results as it's clearly also cavitation nuisance. During experiments and simulations, a number of pressure probes were mounted on the hull over the propeller. The recorded peak to peak variation in the pressure probes increases by about a factor of 10 from non-cavitating to cavitating conditions in the probe located closest to the propeller, in the simulation. In the other probes, the pressure fluctuations are quite modest in the non-cavitating condition while the cavitation imposes an almost identical pressure variation in all studied probes of the aft ship. This behaviour is subject to further investigation, but is expected to be due to the monopole character of the cavitation that was captured in the simulation. In the included figures, this behaviour can be qualitatively assessed by comparing the colouring of the hull and rudder in, e.g., Figures 11b and 11f. In the first of these frames, the blade is in close to top position with a well developed cavity leading to high pressures on the surrounding surfaces, indicated by a light shade of red in the colouring. In the second one, the cavitating blade has moved to around 45°and is thus further from the hull (before a new cavity starts to develop on the approaching blade), and we note a considerably darker colour on the hull and rudder.

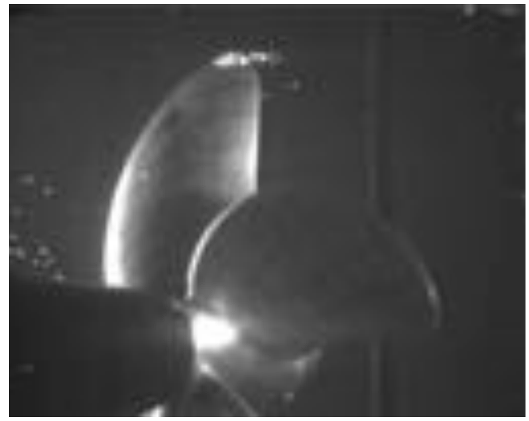

(a)

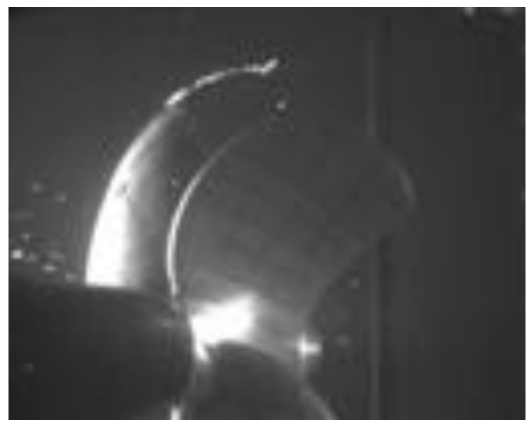

(b)

Figure 10: Snapshots of cavitation in the model tests performed at CNR-INSEAN; condition tested is 13 kns, Kt = 0.2292, and 45 mBar.

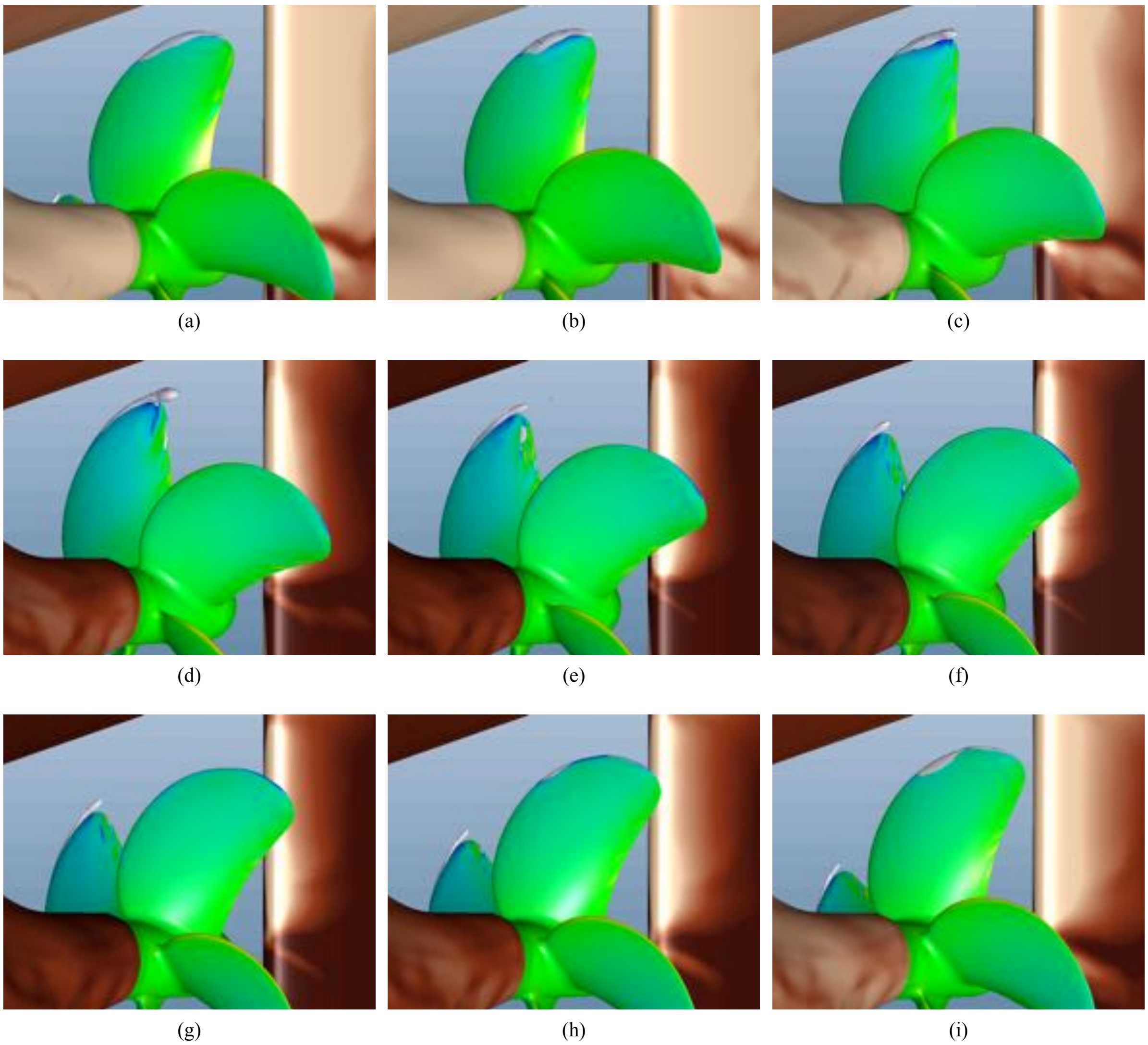

Figure 11: Instantaneous cavitation behaviour for the BL configuration. Cavity extent is indicated by the 95% vapour fraction isosurface, propeller is coloured by pressure where blue indicates vapour pressure. Also the hull and rudder pressure level is indicated by the shade of red, where dark is low pressure and light is high pressure.

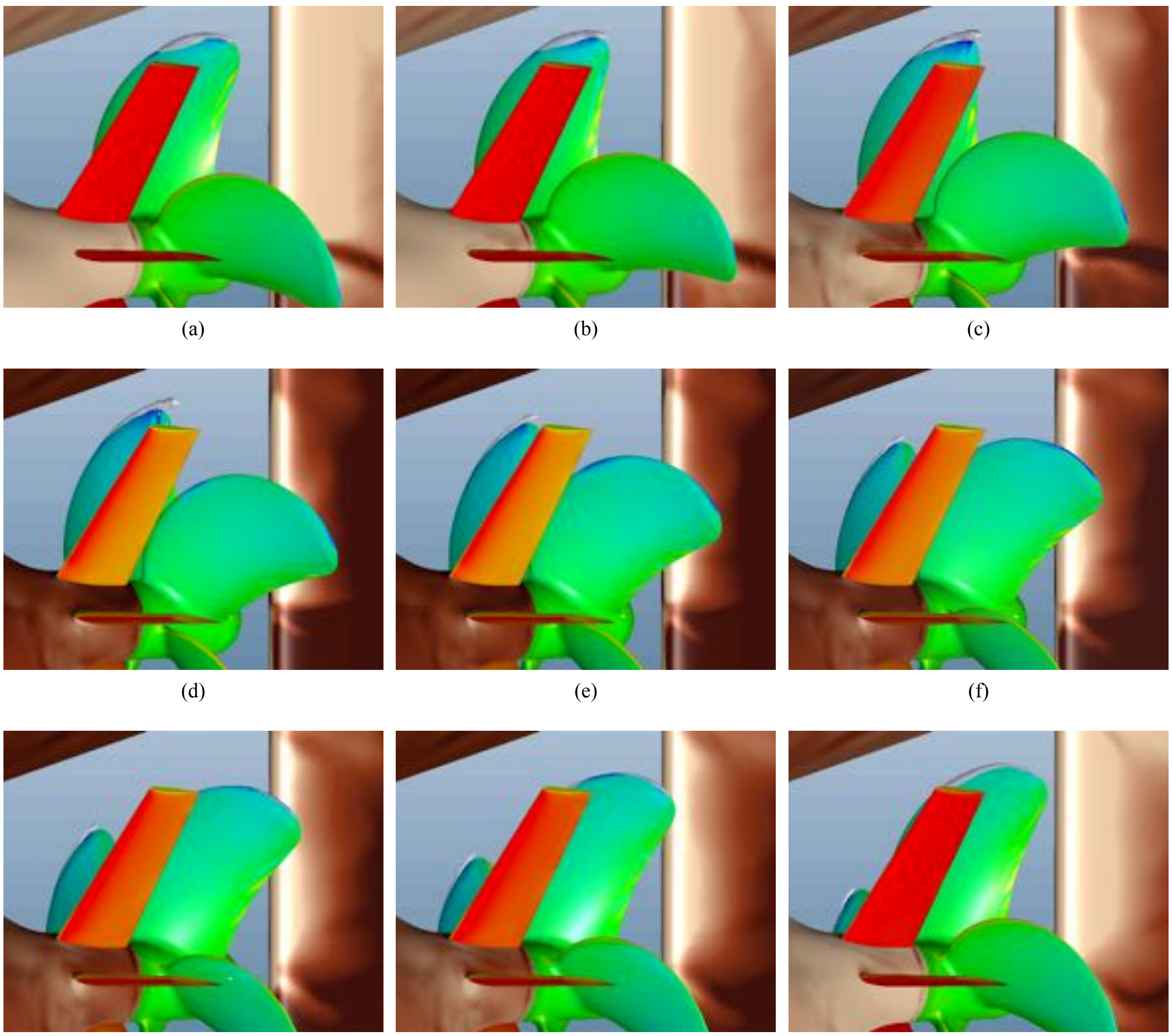

(a) (b) (c) (d) (e) (f) (g) (h) (i)

Figure 12: Instantaneous cavitation behaviour for the PSS configuration. Cavity extent is indicated by the 95% vapour fraction isosurface, propeller and stator blades are coloured by pressure where blue indicates vapour pressure. Also the hull and rudder pressure level is indicated by the shade of red, where dark is low pressure and light is high pressure.

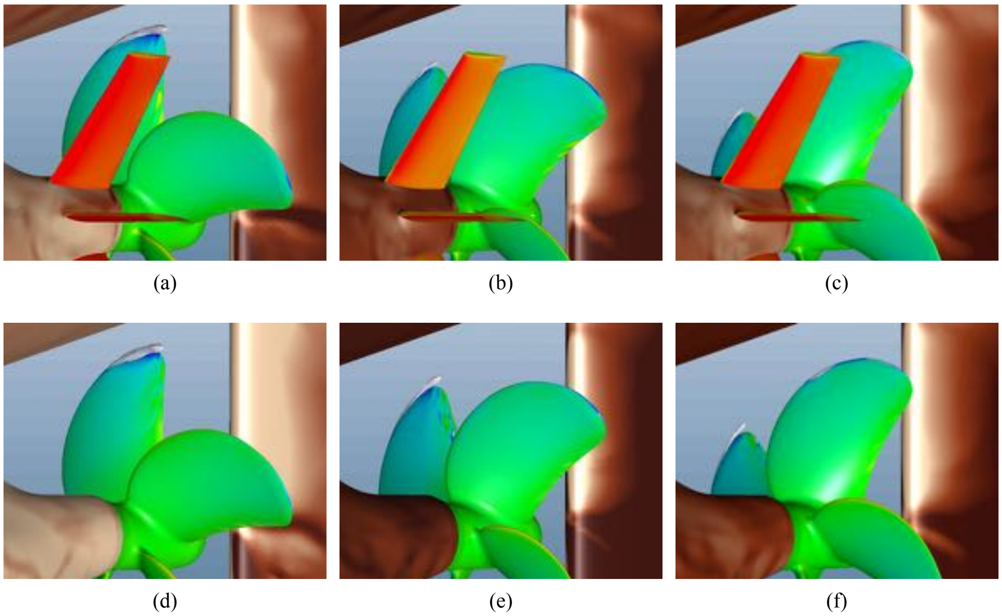

Figure 13: Comparison of the cavitation behaviour between the PSS and the BL configuration. Cavity extent is indicated by the 95% vapour fraction isosurface, propeller and stator blades are coloured by pressure where blue indicates vapour pressure. Also the hull and rudder pressure level is indicated by the shade of red, where dark is low pressure and light is high pressure.

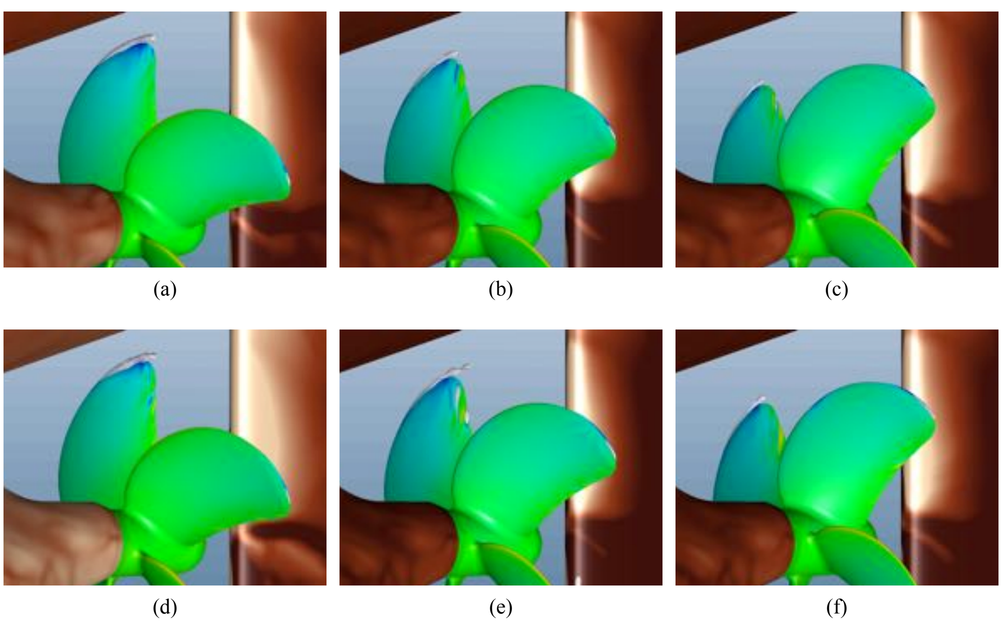

Figure 14: Comparison of the cavitation behaviour between different blade passages in the BL configuration. Cavity extent is indicated by the 95% vapour fraction isosurface, propeller and stator blades are coloured by pressure where blue indicates vapour pressure. Also the hull and rudder pressure level is indicated by the shade of red, where dark is low pressure and light is high pressure.

7 CONCLUSIONS

In this paper, we have presented results from implicit large-eddy simulations of a 7000DWT chemical tanker, with a flow analysis focusing on unsteady propulsor-hull interaction phenomena in a baseline configuration (BL) as well as one with a pre-swirl stator installation (PSS). All studies have been performed in model scale. A complete geometrical propeller model was included in the simulations, using a sliding interface method. Cavitating conditions were simulated based on a single fluid mixture approach with mass transfer modelling according to Kunz et al. (2000). These simulations were complemented by simulations of the towed hull configuration and the propeller in open-water condition. A limited comparison with experimental data was carried out for a number of flow quantities, for the hull-only case, the open-water propeller, as well as for the hull-propeller case in cavitating conditions.

The simulations show good agreement with the experiments in cases with similar conditions and qualitatively display reasonable behaviour for other conditions. From the simulations, it is possible to extract detailed transient flow information to improve the understanding of how the propeller is influenced by the complex hull wake flow and how this changes with the PSS present. For this hull in model scale, a distinct flow separation zone is present just upstream the propeller, which incurs a large variation in propeller blade loading, not only during one propeller revolution but also in between different blade passages. An important feature in the wake flow is the vertical flow component into the propeller plane, significantly responsible for a high variation in blade load during one revolution, perhaps more so than the velocity deficit from the flow separation. A secondary of effect is the development of flow structures entering the blade root area. The former§ effect is noticeably reduced for the PSS, this is the objective with the device. The current configuration is not optimised and a stronger effect could be anticipated in a real commercial design.

The cavitation simulations show a good level of detail for the on-blade cavitation, expected to be sufficient to perform a rudimentary visual erosion risk assessment. The tip vortex propagation has not been possible to predict with this resolution, and this is still a formidable challenge in simulations. This phenomenon is important to be able to predict to make noise predictions and rudder erosion assessment.

The separating flow is expected to decrease significantly in full scale, but this does not necessarily imply that the level of effective wake unsteadiness will decrease significantly. For a correct design of the PSS, full scale simulations are necessary, although the increased knowledge on unsteady flow behaviour gained through these kind of model scale simulations are deemed important. Full-scale investigations of the type illustrated in the present paper are expected to be feasible in the near future.

With the current development of computational capacity, the type of analysis techniques illustrated in the present paper are becoming worthwhile to carry out prior to design in order to understand what flow features govern the propeller operation and the time-resolved behaviour. How to best support the design process with these new analysis tools is however yet to be elucidated, and the authors hope that the present paper can contribute to that development. The simulations results presented in this work clearly illustrates that the instantaneous wake differs significantly compared with the average effective wake, and of course even more so for the nominal wake. This knowledge is relevant not only regarding design requirements on transient features, such as vibration, noise, and cavitation, but also influences integral quantities such as thrust and propulsive efficiency.

Acknowledgements

The authors wish to thank other partners of the STREAMLINE project involved in the investigation of the configuration under study, and its design optimisations, for fruitful scientific discussions concerning how complementary computational and experimental techniques can advance the understanding of unsteady hull-propeller interaction, in particular Dr. Mattias Liefvendahl. We are grateful to CNR-INSEAN, whose staff have been most helpful in connection with the towing tank experiments.

Simulations were performed at C3SE, Chalmers Centre for Computational and Scientific Engineering, on grants allocated by SNIC, the Swedish National Infrastructure for Computing.

This paper was partially supported with funding from the European Union 7th Framework Programme under project STREAMLINE (grant agreement number 233896).

References

Barton, I. E. (1998), ``Comparison of SIMPLE- and PISO-type Algorithms for Transient Flows," Int. J. Num. Meth. Fluids, 26.

Bensow, R. (2013), ``Simulation of Unsteady Propeller Blade Loads Using OpenFOAM," 16^{th} Numerical Towing Tank Symposium, NuTTS'13, Mülheim, Germany.

Bensow, R. and Fureby, C. (2007), ``On the Justification and Extension of Mixed Methods in LES," J. Turbulence, 8.

Bensow, R. and Liefvendahl, M. (2008), ``Implicit and Explicit Subgrid Modeling in LES Applied to a Marine Propeller," AIAA-2008-4144.

Bensow, R. E. and Bark, G. (2010), ``Implicit LES Prediction of the Cavitating Flow on a Propeller," J. Fluids Eng.

Bugalski, T. and Szantyr, J. (2014), ``Numerical Analysis of Propeller-induced Pressure Pulses in Wakes Modified by Improvement Devices," 17 th Numerical Towing Tank Symposium, Marstrand, Sweden.

Calcagni, D., Bellotto, F., Broglia, R., Salvatore, F., and Bensow, R. (2014), ``Comparative analysis of the hydrodynamic performance of conventional and twisted rudders using a hybrid RANSE/BEM model," ISOPE 2014, Busan, Korea.

Chapman, D. R. (1979), ``Computational aerodynamics development and outlook," AIAA Journal, 17, 1293-1313.

Deng, G. B., Queutey, P., Visonneau, M., and Salvatore, F. (2013), ``Ship propulsion prediction with a coupled RANSE-BEM approach." V International Conference on Computational Methods in Marine Engineering, MARIN2013, Hamburg, Germany.

Farrell, P. E. and Maddison, J. R. (2011), ``Conservative interpolation between volume meshes by local Galerkin projection," Comput. Methods Appl. Mech Engrg, 200(89).

Fureby, C. (2008), ``Large Eddy Simulation of Ship Hydrodynamics," 27th Symposium on Naval Hydrodynamics, Seoul, Korea.

Fureby, C., Alin, N., Menon, N., Svanstedt, S., and Persson, L. (2004), ``On Large Eddy Simulation of high Reynolds number wall bounded flows," AIAA Journal, 457.

Grinstein, F., W., L. M., and Rider (eds.) (2007), Implicit Large Eddy Simulation: Computing Turbulent Fluid Dynamics, Cambridge University Press, Cambridge, England.

Kunz, R., Boger, D., Stinebring, D., Chyczewski, T., Lindau, J., Gibeling, H., Venkateswaran, S., and Govindan, T. (2000), ``A preconditioned Navier-Stokes method for two-phase flows with application to cavitation prediction," Comput. Fluids, 29(8).

Liefvendahl, M. and Bensow, R. E. (2014), ``Simulation Based Analysis of Hull-Propeller-Rudder Interaction for a Single-Screw Transport Ship," 30th Symposium on Naval Hydrodynamics, Hobart, Tasmania, Australia.

Patankar, S. V. and Spalding, D. B. (1972), ``A calculation procedure for heat, mass and momentum transfer in three-dimensional parabolic flows," Int. J. Heat Mass Transfer, 15.

Pecoraro, A., Felice, F. D., Felli, M., Salvatore, F., and Viviani, M. (2013), ``Propeller-hull interaction in a single-screw vessel," 3rd Int. Symp. Marine Propulsors, Launceston, Tasmania, Australia.

Piomelli, U. and Balares, E. (2002), ``Wall-layer models for large-eddy simulation," Annual Review of Fluid Mechanics, 34, 349-374.

Queutey, P., Deng, G. B., Guilmineau, E., and Salvatore, F. (2013), ``A comparison between full RANSE and coupled RANSE-BEM approaches in ship propulsion performance prediction." 32nd International Conference on Ocean, Offshore and Artic Engineering, OMAE2013.

Sagaut, P. (2002), Large eddy simulation for incompressible flows., Springer-Verlag.

Turunen, T. (2014), ``Analysis of Multi-Propeller Marine Applications by Means of Computational Fluid Dynamics," Master's thesis, Aalto University.

Van der Ploeg, A. and Foeth, E. (2013), ``OPTIMIZATION OF A CHEMICAL TANKER AND PROPELLER WITH CFD," V International Conference on Computational Methods in Marine Engineering - MARINE2013, Hamburg.

Weller, H., Tabor, G., Jasak, H., and Fureby, C. (1997), ``A Tensorial Approach to CFD using Object Oriented Techniques," Comput. Phys., 12, 620.